Optimising Camera Arrangement for Stereoscopic Particle Image Velocimetry

S.-K. Lee[1,2], M. Giacobello[1], P. Manovski[1] and C. Kumar[1]

[1]Defence Science and Technology Organisation, Melbourne, VIC 3207 AUSTRALIA

[2]University of Tasmania, Launceston, TAS 7250 AUSTRALIA

Abstract

An error model constructed from geometric optics describes the relative error between the out-of-plane and the in-plane (particle) displacements in Stereoscopic Particle Image Velocimetry (SPIV) for a wide range of camera arrangements. Performance charts developed from the model allows the effect of SPIV camera angles on the relative error to be assessed. The model is supplemented with an experimental case study to provide, in the context of large-scale test facilities, practical limits on the SPIV camera angles to reduce vignetting.

Introduction

SPIV is a well-known technique for measuring fluid velocity across a plane of interest within a flow field [1, 2, 3, 4]. The optimal geometric setup for SPIV is generally one where two cameras are symmetrically positioned at $45\degree$ to the imaging or object plane. For many wind-tunnel facilities, this may not be achievable due to optical access constraints. For example, older large-scale facilities built without consideration for optical access required for SPIV, and high-speed wind tunnels built with solid steel walls and limited fixed viewing ports. This study therefore aims to address the implications of working with a non-optimal SPIV setup, and so extends the work of Lawson and Wu [1]. From geometric optics, an error model has been constructed to assess the relative error between the out-of-plane and the in-plane displacements for SPIV measurements. The model is based on thin-lens theory, which excludes optical effects due to the thickness of the lenses so that ray tracing can be simplified. Rotational SPIV arrangements (Fig. 1) are considered and the effect of varying the camera angles (α_1, α_2), both symmetrically and asymmetrically, is analysed. The analysis is supplemented with an experiment to provide practical limits on the camera angles to minimise non-uniform image illumination, known as vignetting.

Rotational SPIV Camera Arrangements

The setup shown in Fig. 1(a), known as a "symmetric rotational" (SR) system, is usually adopted to avoid perspective error [2]. The two cameras are located on the same side of the
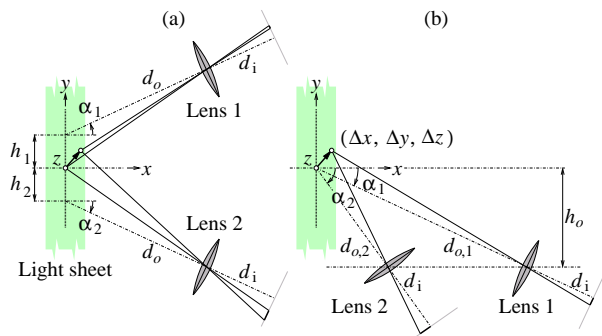

Figure 1. The SPIV system; (a) symmetric rotational (SR) with $\alpha_1 = \alpha_2$ or asymmetric rotational (AR) with $\alpha_1 = 0$ and α_2 adjustable; (b) rotational translational (RT) at a fixed distance h_o.

object plane (light sheet) and are rotated by the same angle but in opposite directions about the system (x) axis. Alternatively, camera 1 may be fixed normal to the light sheet and camera 2 set to an oblique angle — the advantage of this "asymmetric rotational" (AR) setup is that camera 1 alone (with $\alpha_1 = 0$) can provide useful two-component PIV [3].

For the "rotational translational" (RT) setup shown in Fig. 1(b), both cameras traverse along a common axis which is offset by a fixed distance h_o from the system (x) axis. This setup is useful when optical access is restricted to one side of a test facility. The cameras (with viewing angles α_1 and α_2) may be located on the same side of the light sheet as shown in Fig. 1(b) (also see [3]) or one on each side of the light sheet as reported by [4].

Error Analysis

To provide a basis for comparing the different SPIV setups shown in Fig. 1, a common (x, y, z) coordinate system is used. For each camera, the image-to-lens distance is fixed at d_i, the object-to-lens distance $d_{o,l}$ is adjustable with the magnification defined as

$$M_l = \frac{d_i}{d_{o,l}} = \frac{1}{\text{reproduction ratio}}, \qquad l = 1, 2. \qquad (1)$$

Note that to identify each camera the subscript "l" is used when defining a parameter. For example, α_l and h_l define the viewing angle and the y-direction offset, respectively, for camera lens $l = 1, 2$.

For each rotational arrangement shown in Fig. 1, the image produced by the light sheet is distorted in the y direction when the camera position (i.e. α_l, h_l) is changed, and the performance of the system can be measured by the ratio between the x-component (out-of-plane) and the y-component (in-plane) particle-displacement errors, after [1]:

$$e_{\text{system}} = \frac{\sigma_{\Delta x}}{\sigma_{\Delta y}}, \qquad (2)$$

where $e_{\text{system}} = 1$ is desirable to avoid bias performance. In the following discussion, the expressions for e_{system} are derived by using the method of transform coordinates (also see [1]).

Symmetric and Asymmetric Rotational (SR, AR) Systems

For the SR setup (Fig. 1(a)), the camera angles are $\alpha_1 = \alpha_2 = \alpha$, where $0 < \alpha < 90\degree$. For simplicity, the performance is considered along the y axis at the light-sheet coordinates $x = z = 0$, and the cameras are assumed to have the same object distance d_o, offset $h_1 = h_2 = 0$ and magnification $M_1 = M_2 = M$. The error ratio (e_{SR}) as a function of α and y/d_o is

$$e_{\text{SR}} = \sqrt{\frac{\cos^2(\alpha)[1 + (y/d_o)^2 \sin^2(\alpha)]}{\sin^2(\alpha) + (y/d_o)^2 \cos^4(\alpha)}}. \qquad (3)$$

For $y = 0$, Eq. (3) simplifies to

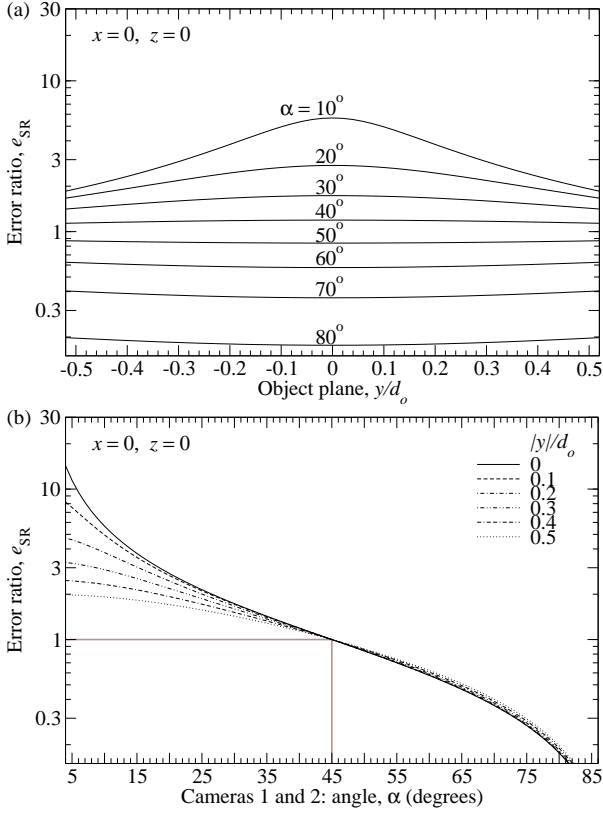$$e_{\text{SR}} = \frac{1}{\tan(\alpha)}. \qquad (4)$$

Figure 2. SR performance charts; Eq. (3).

Figure 3. AR performance charts; Eq. (5).

A plot of Eq. (3) in Fig. 2(a) shows that the distribution of e_{SR} is symmetric about the centre of the object plane; e_{SR} decreases as α is increased. Fig. 2(b) shows that $\alpha = 45°$ gives the best performance, where $e_{\mathrm{SR}} = 1$ is independent of the y location.

The AR setup is slightly different from the SR setup in Fig. 1(a), where camera 1 is fixed ($\alpha_1 = 0$; $h_1 = 0$) and camera 2 is adjustable ($0 < \alpha_2 < 90°$; $h_2 = 0$). For $x = z = 0$, the error ratio as a function of α_2 and y/d_o for this system is

$$e_{\mathrm{AR}} = \sqrt{\frac{1 + \cos^2(\alpha_2)[1 - (y/d_o)\sin(\alpha_2)]^2}{(y/d_o)^2 + [\sin(\alpha_2) + (y/d_o)\cos^2(\alpha_2)]^2}}. \quad (5)$$

For $y = 0$, Eq. (5) reduces to

$$e_{\mathrm{AR}} = \sqrt{\frac{1 + \cos^2(\alpha_2)}{\sin^2(\alpha_2)}}. \quad (6)$$

A plot of Eq. (5) in Fig. 3(a) shows an asymmetric error-ratio distribution. As α_2 approaches $90°$, the error ratio tends to unity (Fig. 3(b)) but in practise the area of the light sheet projected onto the camera is significantly reduced. Also, the local magnification across the image plane becomes highly non-uniform (e.g. see [2], Fig. 5). It is possible to minimise image distortion while keeping the error ratio close to unity by setting the camera viewing angle at approximately mid-way between the two opposing requirements, i.e. $\alpha_2 \sim 35°\text{-}55°$.

Rotational Translational (RT) System

For the RT setup shown in Fig. 1(b), the ratio d_i/h_o is the same for both cameras and so, to acquire the same target area on the object plane, each lens requires a different image magnification:

$$M_l = \frac{d_i}{d_{o,l}} = \frac{d_i}{h_o}\sin(\alpha_l), \qquad l = 1, 2, \quad (7)$$
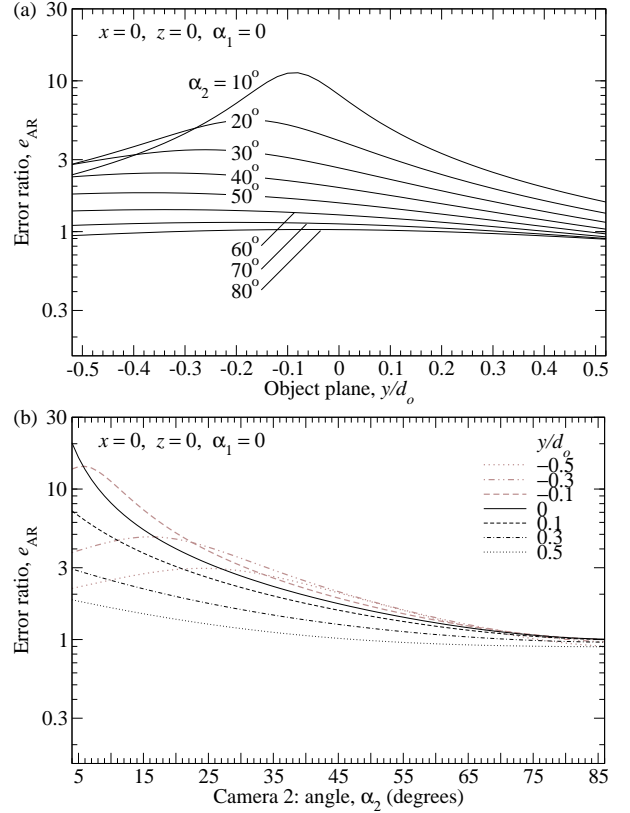
where, for cameras on the same side of the light sheet,

$$0 < \alpha_1 < \alpha_2 < 90°, \quad (8)$$

and for cameras on opposite sides of the light sheet,

$$0 < \alpha_1 < 90° \quad \text{and} \quad 90° < \alpha_2 < 180°. \quad (9)$$

To avoid having the camera in the path of the light sheet, a viewing angle of $90°$ is avoided. For $x = z = 0$, the error ratio as a function of α_1, α_2 and y/h_o for this system is

$$e_{\mathrm{RT}} = \sqrt{\frac{\begin{array}{c}[\cos(\alpha_1)\sin(\alpha_1)]^2[1 - (y/h_o)\sin^2(\alpha_1)]^2 + \\ [\cos(\alpha_2)\sin(\alpha_2)]^2[1 - (y/h_o)\sin^2(\alpha_2)]^2\end{array}}{\begin{array}{c}\sin^4(\alpha_1)[1 + (y/h_o)\cos^2(\alpha_1)]^2 + \\ \sin^4(\alpha_2)[1 + (y/h_o)\cos^2(\alpha_2)]^2\end{array}}}. \quad (10)$$

Figure 4 shows a plot of Eq. (10) for the case $\alpha_1 = 35°$; camera angles in the range $15° \le \alpha_1 \le 55°$ produce very similar trends. For $y = 0$, Eq. (10) simplifies to

$$e_{\mathrm{RT}} = \sqrt{\frac{[\cos(\alpha_1)\sin(\alpha_1)]^2 + [\cos(\alpha_2)\sin(\alpha_2)]^2}{\sin^4(\alpha_1) + \sin^4(\alpha_2)}}. \quad (11)$$

Figure 5(a) shows a plot of Eq. (11). For camera 1 with a known angle of α_1, Eq. (11) gives $e_{\mathrm{RT}} = 1$ when camera 2 has the following angle (Fig. 5(b)):

$$\alpha_2 = \sin^{-1}\sqrt{\frac{1 + \sqrt{1 + 8\left[\cos^2(\alpha_1)\sin^2(\alpha_1) - \sin^4(\alpha_1)\right]}}{4}}, \quad (12)$$

which gives the locus of optimum performance for the RT setup. For camera 1 in the range $0 < \alpha_1 < 45°$, there are two possible
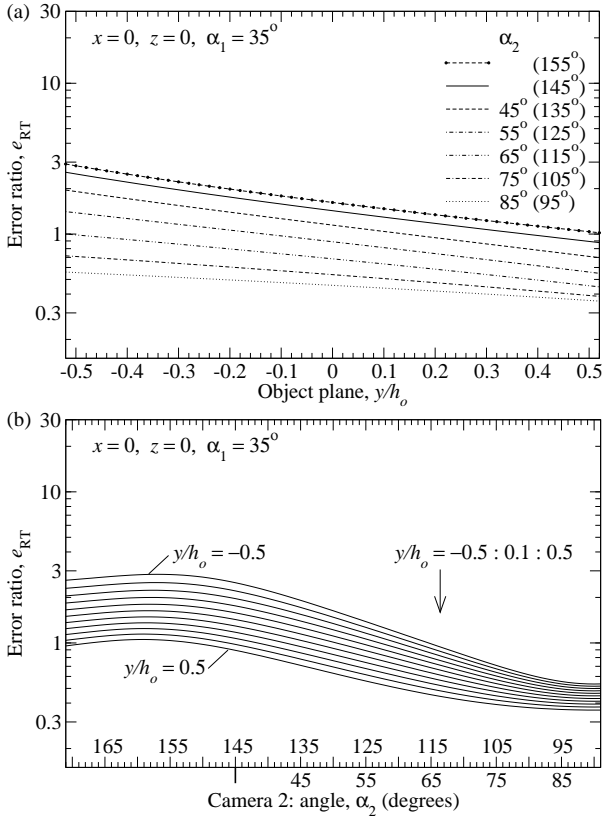
(a) ... (graph)

(b) ... (graph)

Figure 4. RT performance charts; Eq. (10) with $\alpha_1 = 35°$.
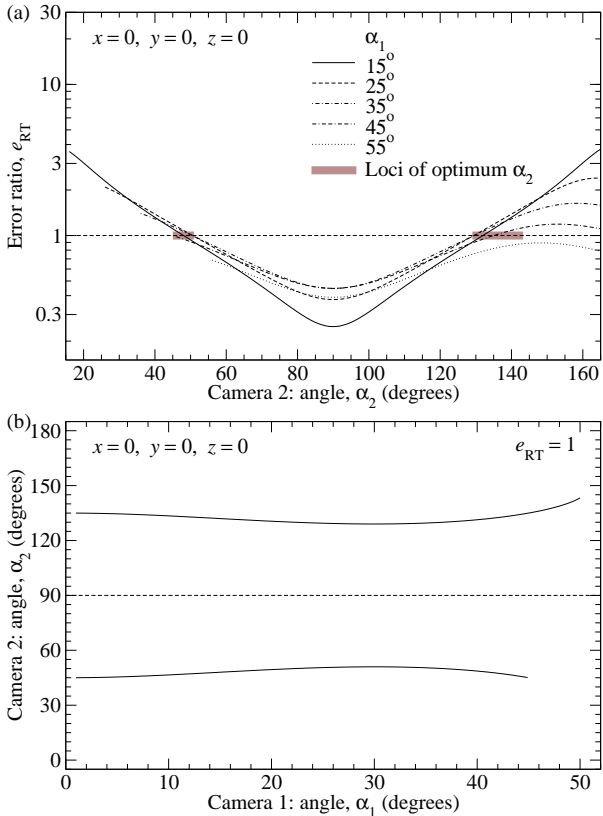

(a) ... (graph)

(b) ... (graph)

Figure 5. Loci of optimum RT camera angles; (a) Eq. (11) and (b) Eq. (12).

viewing angles for camera 2, as indicated by the shaded regions in Fig. 5(a). A plot of Eq. (12) in Fig. 5(b) shows that the locus curves are symmetrically distributed about the horizontal line $\alpha_2 = 90°$. For camera 1 with a viewing angle in the range $0 < \alpha_1 < 45°$, the optimum viewing angle for camera 2 falls in the range $45° < \alpha_2 < 51°$ on the same side of the light sheet or in the range $129° < \alpha_2 < 135°$ on the opposite side.

A Practical Case Study of Vignetting

For each camera to achieve sharp focus of the object plane, the depth-of-field needs to be adequate to account for variation in the object distance. The depth-of-field improves by increasing the f-stop but this reduces the amount of light registered by the camera. Alternatively, a sharp corner-to-corner focus can be achieved by tilting the camera (charge-coupled device, CCD) sensor horizontally (i.e. in the y direction) by a small angle, after [5, 6]:

$$\theta_l = A_l \times G_l \times \theta_{s,l}, \qquad (13)$$

where $A_l = (1 + (y/d_{o,l})^2)^{-2}$ is an illumination factor, G_l is a geometric vignetting factor which depends on the camera assembly (i.e. the housing for the lens and the camera), and $\theta_{s,l} = \tan^{-1}[M_l \tan(\alpha_l)]$ is the Scheimpflug [5] condition.

The remainder of this section describes an experiment to demonstrate Eq. (13), where G_l is specific to the SPIV setup. For simplicity, the target plane (a matte whiteboard with a horizontal ruler printed to scale) is uniformly illuminated. The distance between the target and the camera is sufficiently large such that $A_l \simeq 1$ and vignetting is not caused by the camera viewing angle α_l. For this experiment, α_l is achieved by tilting the target plane about its vertical centreline axis.

Typically, in the context of performing SPIV in large-scale facilities, the distance between the cameras and the target plane is substantial. To reflect this in the present experiment, the target (whiteboard/ruler) is viewed through a 200 mm Micro-Nikkor lens at a fixed distance $d_{o,l} = 2300$ mm with an f-stop of 8 (to provide adequate depth-of-field). The image is captured by a TSI PowerView Plus (11 mega-pixel) camera. Each image (4008-pixels × 2672-pixels size) has a spatial resolution of 0.104 mm/pixel and is recorded in 12-bit tagged image file format (TIFF). The nominal magnification is determined by the ratio between the width of the camera sensor ($y_i = 36$ mm) and the image of the horizontal ruler ($y_{o,l} = 408$ mm) recorded on the sensor, i.e. $M_l = y_i/y_{o,l} = 36/408 = 0.09$.

Figure 6 shows typical images of the ruler for a range of tilt angles (θ_l) at $\alpha_l = 35°$; camera angles in the range $30° \leq \alpha_l \leq 50°$ produce similar images. Note that adjusting θ_l alters the corner-to-corner sharpness of the image through the intensity of the graduations on the ruler, and so the distribution of intensity along the ruler provides a measure for sharpness.

To assess the effect of vignetting, horizontal distributions of intensity are taken from the blank portion of the whiteboard. Figure 7(a) shows the variation in the image intensity for a range of tilt angles (θ_l). The intensity is non-dimensionalised by the nominal peak value (of the whiteboard) registered by the camera. The trends in Fig. 7(a) are independent of the camera viewing angle tested in the range $30° \leq \alpha_l \leq 50°$. That is, the falloff in intensity is due to an increase in the tilt angle (θ_l) only; increasing θ_l from 0 to 4.0° produces a maximum intensity falloff of approximately 40% (on the left-side of the image). Figure 7(b) shows that it is possible to reduce vignetting by shifting the camera (CCD) sensor along the y direction. For the present setup, a horizontal shift of -3 mm (i.e. $\Delta y/d_o = -3/2300 = -1.3 \times 10^{-3}$) recovers approximately 6% of the intensity on the left corner.
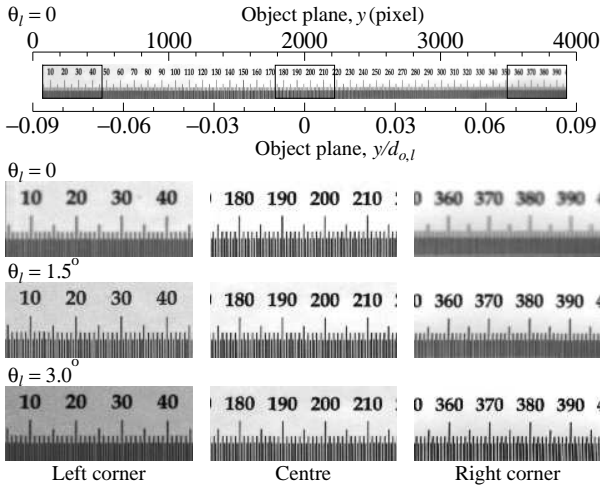
Figure 6. Effect of tilt angle (θ_l) on corner-to-corner sharpness and vignetting (intensity falloff) on the left corner. $\alpha_l = 35°$, $d_{o,l} = 2300\,\text{mm}$, $M_l = 0.09$ and f-stop $= 8$.
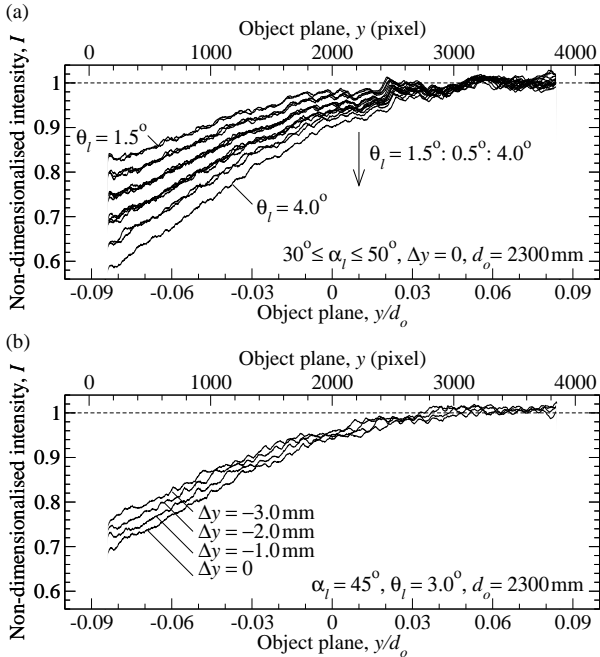

Figure 7. Non-dimensionalised image intensity, I, showing the effect of vignetting due to (a) horizontal tilt θ_l and (b) shift Δy of the camera (CCD) sensor. $M_l = 0.09$ and f-stop $= 8$.

Figure 8 shows the tilt angle θ_l as a function of the camera setting "$M_l \times \tan(\alpha_l)$", where the locus of optimum corner-to-corner sharpness (data shown as "$\triangle$") is determined by visual inspection of the ruler images (Fig. 6). A least-squares fit of Eq. (13) to the locus points ("$\triangle$") yields $G_l = 0.6$.

The maximum intensity falloff shown in Fig. 7 is plotted in Fig. 8 as a function of the tilt angle θ_l. From Fig. 7, measurements obtained with no camera shift $\Delta y = 0$ are shown as data points "$\bigcirc$" in Fig. 8; for the case with a camera shift of $\Delta y = -3\,\text{mm}$, the measurement is shown as "$+$" and a different horizontal scale is used in Fig. 8 to plot the maximum intensity falloff. For example, with $\alpha_l = 45°$ and $M_l = 0.09$, the tilt angle required to achieve corner-to-corner image sharpness is $\theta_l = 3.0°$. This corresponds to a maximum intensity falloff of 30% for $\Delta y = 0$. With a camera shift of $\Delta y = -3\,\text{mm}$ (for the present system), the falloff is reduced to 24%.
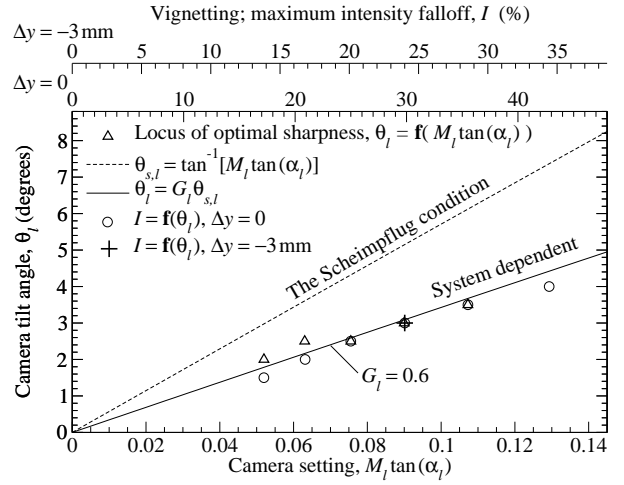

Figure 8. Performance of camera tilt and shift (with 200-mm lens) — locus of optimal corner-to-corner image sharpness. $d_{o,l} = 2300\,\text{mm}$, $M_l = 0.09$ and f-stop $= 8$.

Concluding Remarks

The use of SPIV is to reduce perspective error and to resolve both out-of-plane and in-plane components of particle displacement from an imaging plane, and so the ratio between the out-of-plane and in-plane displacement errors is a key performance parameter. Geometric analysis establishes the error ratio as a function of SPIV camera viewing angles (α_l) and from this, performance charts are developed to allow assessment of non-optimal camera arrangements (i.e. error ratio $\neq 1$). The error model is supplemented with experiment data to provide, for a given SPIV system, practical limits on the camera tilt angle (θ_l) and shift (Δy) to reduce vignetting.

Acknowledgements

References

[1] Lawson, N. J. & Wu, J. Three-dimensional particle image velocimetry: error analysis of stereoscopic techniques. *Measurements, Science and Technology*, 1997, 8:894–900.

[2] Prasad, A. K. Stereoscopic particle image velocimetry. *Experiments in Fluids*, 2000, 29:103–116.

[3] Di Felice, F. & Pereira, F. *Developments and applications of PIV in Naval Hydrodynamics*. In *Particle image velocimetry, Topics in Applied Physics, 2008, 112:475–503*. (Eds. Schroeder, A. & Willert, C., Springer-Verlag, 2008).

[4] Willert, C. Stereoscopic digital particle image velocimetry for application in wind tunnel flows. *Measurements, Science and Technology*, 1997, 8:1465–1479.

[5] Scheimpflug, T. Improved method and apparatus for the systematic alteration or distortion of plane pictures and images by means of lenses and mirrors for photography and for other purposes. British Patent No. 1196, 1904.

[6] Kang, S. B. & Weiss, R. Can we calibrate a camera using an image of a flat, textureless Lambertian surface? *European Conference on Computer Vision*, 2000, vol. II, 640–653.